High contrast at small separation - III. Impact on the dark hole of MEMS deformable mirror control electronics

P. Martinez, M. Beaulieu, L. Abe, P. Baudoz, C. Gouvret, A. Spang, A. Marcotto

Monthly Notices of the ROYAL ASTRONOMICAL SOCIETY

MNRAS **532,** 2892–2904 (2024) https://doi.org/10.1093/mnras/stae1677
Advance Access publication 2024 July 12

High contrast at small separation – III. Impact on the dark hole of MEMS deformable mirror control electronics

P. Martinez,[1]★ M. Beaulieu,[1] L. Abe,[1] P. Baudoz,[2] C. Gouvret,[1] A. Spang[1] and A. Marcotto[1]

[1]*Université Côte d'Azur, Observatoire de la Côte d'Azur, CNRS, Laboratoire Lagrange, Bd de l'Observatoire, CS 34229, 06304 Nice cedex 4, France*
[2]*LESIA, Observatoire de Paris, PSL Research University, CNRS, Sorbonne Universités, UPMC Univ. Paris 06, Univ. Paris Diderot, Sorbonne Paris Cité, 5 place Jules Janssen, 92195 Meudon, France*

Accepted 2024 July 4. Received 2024 June 28; in original form 2024 February 14

ABSTRACT

The creation of a dark hole (DH) region in the science image for exoplanet direct detection depends on deformable mirrors (DMs), where the imperfect control of DM limits the achievable contrast. The mirror surface height resolution is set by the DM drive electronics, and the quantization errors in DM impact the contrast in the DH. Consequently, determining the optimal voltage value for the flattening map of DM is essential, as it involves balancing dynamic and accuracy considerations. We conduct a numerical study to examine the impact of these parameters on microelectromechanical DM within the high-contrast field of view of several DHs with various characteristics and optical configurations. Our analysis includes an exploration of their influence on both small and moderate angular separations. We compare our numerical results with a formula available in the literature that aims to capture the dependence of contrast on DM quantization errors. We show that the formula accuracy to predict the contrast limit when the DM deflection curves follow the as-manufactured quadratic power law is dependent on the DM flattening map voltage domain, regardless of DH size and angular separations. Further these results appear to be insensitive to factors such as actuator number, coronagraph type, set-up architecture, and science objective (small or moderate angular separations). We provide guidelines for determining the optimal voltage for the DM flattening map, discuss the domain validity of the formula used to predict DM quantization errors on the contrast, and provide insights into balancing DM actuator density and mirror surface height resolution.

Key words: instrumentation: miscellaneous – methods: numerical – techniques: high angular resolution – techniques: miscellaneous.

1. INTRODUCTION

The ultimate science case for observing Earth-like planets orbiting stars in their habitable zone requires image contrast in visible light on the order of 10^{-10} at short orbits from the host star. To address this goal, a leading approach combines high-performance coronagraphy and wavefront shaping to reduce starlight and generate a dark region within the image, enhancing the exoplanet signal to noise. Coronagraphs are designed to suppress diffracted light but require exquisite image quality. Wavefront errors in the telescope and instrument optics diffract starlight, and if left uncorrected, create speckle noise in the focal plane, overwhelming the planet signal in the coronagraphic image by order of magnitude. Active control of the optical wavefront is essential, and deformable mirrors (DMs) are critical devices undergoing constant development for use in space-based coronagraph instruments and ground-based observatories. Multi-DM control is extensively tested worldwide across various laboratory test-beds (e.g. THD—Galicher et al. 2014, HCIT—Riggs et al. 2013, HCIL—Pueyo et al. 2011; Riggs et al. 2013, HiCAT—N'Diaye et al. 2013, and SPEED—Martinez et al. 2014). A set of DMs corrects wavefront errors of imperfect optical surfaces and shapes the wavefront to produce a dark zone, namely the dark hole (DH), in the science image halo. Various successful laboratory experiments using either a single DM (e.g. Trauger & Traub 2007; Belikov et al. 2010; Guyon et al. 2010; Mazoyer et al. 2014; Delorme et al. 2016) or two DMs (e.g. Kay, Pueyo & Kasdin 2009; Pueyo et al. 2011; Riggs et al. 2013) have demonstrated the relevance of the technique. Among the critical aspects of DM technologies, the drive electronics are essential because they define the minimal step of DM surface motion and how well we can control them. In this context, DM electronics have become a subject of study, with several authors (e.g. Trauger et al. 2007; Traub & Oppenheimer 2010; Trauger et al. 2011; Bendek et al. 2020; Ruane et al. 2020) attempting to predict the impact of DM quantization errors on the contrast in the DH. Multiple studies provide predictions and recommendations for setting specifications on DM control electronics (Ruane et al. 2020) to achieve the 10^{-10} contrast requirement for imaging Earth-like planets. Among the existing DM technologies, microelectromechanical systems (MEMS) are widely used in ground-based high-contrast imaging observatories and are being considered for space missions. Further, MEMS DMs are the most commonly used wavefront shaping solutions for laboratory coronagraph test-beds.

★ E-mail: patrice.martinez@oca.eu

Robust requirements for the DM surface height resolution are mandatory for future coronagraph instruments. A simple and widely used approximate formula is available in the literature (Traub & Oppenheimer 2010; Ruane et al. 2020) to capture the dependence of contrast on DM quantization errors. While it is firmly established that DM quantization errors can set the limit for achievable contrast in a DH region (Ruane et al. 2020), the equation's domain of validity remains an open question. Specifically, the impact of DM quantization errors at small angular separations compared with moderate/large orbits is left unexplored to our knowledge. On the other hand, while the DM drive electronics determine the minimal surface motion step achievable in practice, the voltage value around which the flattening map of the DM is defined is also crucial. It defines the available dynamic range and accuracy a DM can achieve because actuators follow a quadratic power-law response with voltages. This is particularly critical when generating a DH region. The process of creating a DH in the science image relies on the DM and can be generalized as a three-step procedure for generality: (i) The first step involves flattening the DM, requiring a nominal voltage map that mostly removes the natural defocus shape of the mirror surface; (ii) the second step is flattening the wavefront entering the coronagraph (non-common path corrections); and (iii) finally, DH creation itself, including sensing methods (e.g. pair-wise probing; Give'on et al. 2007) to reconstruct the electric field and methods [e.g. electric field conjugation (EFC); Groff 2012; Riggs et al. 2013; Ahn et al. 2023; Haffert et al. 2023) to cancel it. In all these steps, dynamic range (stroke available) and accuracy (the smallest amount an actuator can be moved) are of primary importance. Flattening a DM to remove low-order aberrations that appear when the DM is unpowered requires a nominal voltage map ranging from 20 to 100 V (peak to valley; PV). It is commonly observed that after running the EFC algorithm to create the DH, the nominal voltage map changes by only a few volts. This highlights the importance of selecting the nominal voltage value for the DM offset map.

In a previous study (Beaulieu et al. 2017), we developed an end-to-end simulator for a generic high-contrast architecture aimed at determining the optimum wavefront control for high-contrast imaging at small separations. This involved the combination of coronagraphy and wavefront shaping using two DMs. The generic set-up assumed a perfect coronagraph, a monolithic circular aperture without central obscuration or spiders, etc. The goal was to assess the impact of the location of the two DMs on wavefront shaping, assuming Fresnel propagation of standard aberrated optics. In a subsequent analysis (Beaulieu et al. 2020), we improved the realism of our instrument set-up design to delve deeper into the assessment. This included an examination of the relative impact of various set-up parameters, such as non-uniform source, residual pupil phasing aberrations, highly aberrated optics, realistic DMs, and coronagraphs. The analysis was carried out with a segmented and obstructed pupil.

The objective of this paper is to use our versatile end-to-end simulator to explore the impact of DM quantization errors and the voltage of DM flattening maps on the contrast in the DH. We compare the contrast impact in scenarios ranging from a small field of view (FoV) at a small inner working angle (IWA) DH to moderate and/or large IWA with wide FoV DH situations. Our aim is to investigate the dependence of quantization errors and initial voltage maps on small/moderate angular separation DH. The obtained results are then compared with predictions generated by a simple and widely used formula proposed by several authors (Trauger et al. 2007, 2011; Traub & Oppenheimer 2010; Ruane et al. 2020). This study is centred around the SPEED test-bed (coronagraph, segmented/obstructed pupil, optical design, etc.; Martinez et al. 2023). We use SPEED as a typical instrument, ensuring that the results can be applied to other high-contrast test-beds due to the shared set-up parameters. To our knowledge, the impact of DM quantization errors on contrast in a DH has not been systematically explored, particularly as a function of the initial DM flattening map voltage. Furthermore, the validity of contrast predictions in a DH with DM quantization errors has never been investigated for both in and out-of-pupil plane DM configurations. This study considers a two-DM set-up architecture and examines the impact of DH size.

The general assumptions for the analysis, including DM drive electronics theory, quantization errors, and the theoretical contrast limits, are detailed in Section 2. Section 3 outlines the numerical assumptions of our end-to-end simulator, the SPEED test-bed, and the realistic assumptions and open parameters used for the analysis. Section 4 presents the results, and finally, we conclude with a summary.

2. THEORETICAL TREATMENT

2.1 DMs electronics

Various DM technologies are routinely used or under development, with one of the most common being MEMS (Bifano, Cornelissen & Bierden 2010; Bierden et al. 2011; Bierden, Cornelissen & Ryan 2014; Morgan et al. 2019). MEMS DMs are metal-coated thin-membrane mirrors whose shape is controlled by an array of electrostatic actuators. The mirror comprises a membrane deformed by a specific number of actuators, each of which can be individually controlled. The local surface displacement (mechanical displacement) is determined by the voltage applied to each actuator, where these actuators provide a displacement practically limited to a few micrometres (referred to as the stroke) over a compact area. In addition to the architecture of MEMS DMs, time-delay response and precision are constrained by the electronics. Standard driver electronics enable 14-bit control; however, increased resolution is possible, particularly if improved accuracy is desired. For the sake of clarity and to illustrate the impact of DM drive electronics, we assume the use of a specific DM in the SPEED experiment (Martinez et al. 2023): the Boston Micromachines Kilo-C DMs. While the numerical values may differ for other DM configurations, the reasoning is applicable across different set-ups.

The Kilo-C DM from the Boston Micromachines vendor (Bierden et al. 2011) has 952 actuators with an inter-actuator spacing of 300 μm, providing a 1.5-μm stroke. The DMs are controlled using 14-bit electronics, with a precision of 14 bits over the full range of the driver (0–300 V) but truncated to the maximum mirror value of 195 V. Scaling the value allows us to determine the number of steps in this range. Scaling 2^{14} over the full 300 V range and the truncated value of 195 V results in approximately 10 650 steps. Since DMs have a maximum displacement of 1.5 μm, the average step size is around 0.1 nm. However, the physical step size value depends on where along the deflection curve the actuators are because MEMS-based DMs have, approximately, a quadratic relationship between the voltage applied and its corresponding deflection (see Fig. 1, obtained from a Kilo-C DM from Boston Micromachines manufacturer, which shows the deflection, denoted as δ, as a function of the voltages.). When the mirror is first deflected, the step size is minimal. As the mirror is deflected further, the size of the step increases as the mirror reaches the middle range region of the curve. Then, at the high end of the curve, the step size becomes larger until the range is exhausted. In practice, it is mandatory to calculate the size of the step for each

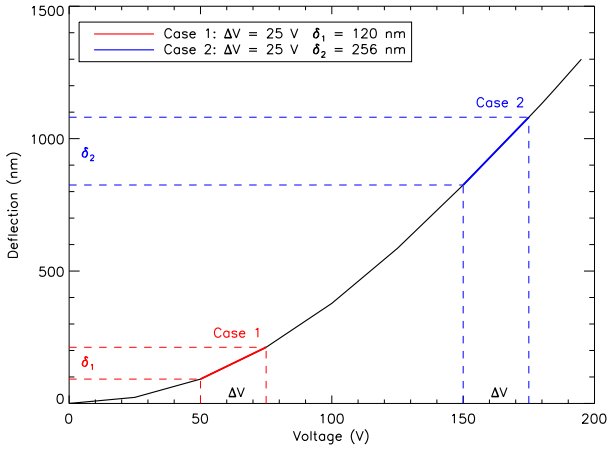

Figure 1. The principle of the actuator deflection curve where the actuator's physical displacement is expressed in nanometre as a function of the applied voltages. The deflection follows a quadratic power law with voltages. In Case 1 and 2, sharing the same voltage variation (ΔV), there is an unequal corresponding displacement of the actuators ($\delta_1 \neq \delta_2$). This discrepancy illustrates that the physical step size value depends on the position along the deflection curve where the actuators are located.

of these ranges using the DM data provided by the manufacturer, as illustrated in Fig. 1.

Fig. 1 presents the basic principle where two situations with equal voltage variations (denoted ΔV) are compared at different locations on the deflection curve: The corresponding actuator displacements (δ_1 and δ_2) differ significantly. Equality of the displacement can only be achieved ($\delta_1 = \delta_2$) by assuming a hypothetical linear power law of the displacement with voltages. We note that, aside from the challenge of achieving the minimal possible step, the stroke error (the disparity between the specified and actual actuator position) can be substantial and greatly influenced by the variability in the maximum range of the electronics amplifiers. This results in various amounts of error at different points along the discussed curve. Addressing the impact on actuator displacement would require measurement and potential compensation, possibly involving the creation of individual curves for each actuator. However, this aspect is not considered in our study. Additionally, actuator stability (referring to the ability of the actuators to hold their shape over time; Morzinski et al. 2006) and repeatability (referring to the ability of the actuator to return to the same position under the same applied voltage consistently; Morzinski et al. 2008) are critical but are beyond the scope of this study.

2.2 Contrast in a DH

A simple formula attempting to capture the impact of DM quantization errors on the contrast in the DH has been proposed by Trauger et al. (2007) and is widely used (Trauger et al. 2011; Bendek et al. 2020; Ruane et al. 2020). For clarity, we will discuss few of the assumptions behind this formula, while a complete mathematical/physical justification is provided in Appendix A. The formula relies on following main assumptions:

(i) Assumption 1: A generic coronagraph instrument, which consists of a DM in a pupil plane, a focal plane, a Lyot stop (LS) in a subsequent pupil plane, and finally a detector plane where the final high-contrast image is recorded.

(ii) Assumption 2: There is a single and unique DM correction at the pupil plane, with an entrance aperture A, an initial aberrated field ϕ (representing both phase and amplitude errors), and the DM perturbation $\psi_{\rm DM}$. The electric field at the pupil plane is then given by

$$E_{\rm p}(u, v) = A(u, v) \exp^{i\phi} \exp^{i\psi_{\rm DM}(u,v)}, \tag{1}$$

where u and v are the spatial coordinates at the pupil plane. In these circumstances, the coronagraph is described as the linear operator C from the pupil plane to the image plane, such that the final electric field is given by

$$E_{\rm f}(x, y) = C\left[E_{\rm p}(u, v)\right], \tag{2}$$

where x and y are the spatial coordinates at the image plane. For small aberration, the pupil electric field is defined as

$$E_{\rm p}(u, v) = 1 + iA\phi - \frac{1}{2}A\phi^2. \tag{3}$$

(iii) Assumption 3: Perfect coronagraph is assumed and it removes the deterministic (constant) term but cannot correct for the linear term $iA\phi$ nor for the quadratic amplitude term $\phi^2/2$ (it cannot correct for the phase contribution).

(iv) Assumption 4: It is also assumed that the DM is in a state where the DH is created, minimizing the normalized intensity.

Under these conditions (i, ii, iii, and iv), Trauger et al. (2007) proposed an analytical relation to quantify the required control accuracy on the DM for a given contrast ($\mathscr{C}$) in terms of the reflected wavefront root mean square (RMS) error ($h_{\rm rms}$) by

$$\mathscr{C} = \pi \left(\frac{8h_{\rm rms}}{N\lambda}\right)^2, \tag{4}$$

where, N represents the number of actuators on the DM evaluated across the pupil diameter, and λ is the wavelength. The assumptions behind this equation are based on (i) the description of stellar intensity in the presence of a coronagraph, assuming that the phase ϕ can be represented as the sum of many sinusoidal ripples (a sum of sine and cosine waves, as per the standard result from Fourier analysis); (ii) the small aberrations regime; and (iii) a modal argument on the control of scattered light with a DM. The complete derivation of equation (4) under these assumptions (i, ii, and iii) is provided in Appendix A.

From equation (4), and by assuming that quantization errors are uniformly distributed,

$$h_{\rm rms} = \frac{h_{\rm min}}{\sqrt{12}}, \tag{5}$$

we can derive the equation as proposed in Ruane et al. (2020) that expresses the contrast as

$$\mathscr{C} = \frac{16\pi}{3}\left(\frac{h_{\rm min}}{N\lambda}\right)^2. \tag{6}$$

It is important to note that this equation ignores factors such as DH size, multiple DM architecture, out-of-pupil plane DM configuration, and DM actuator shape or influence function, which may impact the distribution of stellar intensity in the focal plane. The effect of the actuator influence function on equation (6) is, however, addressed in Ruane et al. (2020), where the formalism is extended to this specific case. In this study, we aim to explore the accuracy and validity of their predictions for both in and out-of-pupil plane DM configurations,

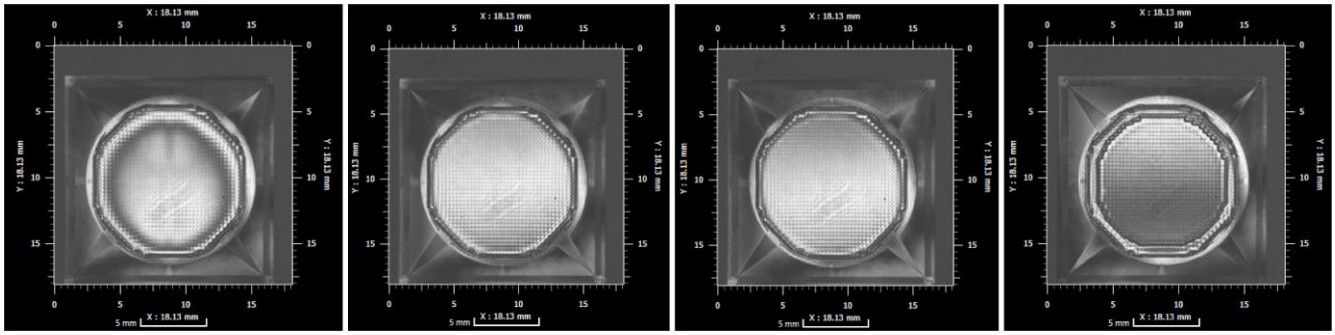

Figure 2. The RMS of the DM surface shape during the flattening process was evaluated for various voltage maps. The optimal set of flattening voltages was determined iteratively using a Zygo interferometer. From left to right, the images show the unpowered shape (RMS 107 nm), a 50 V flattening map (RMS 10 nm), a 60 V flattening map (RMS 10 nm), and a 150 V flattening map (RMS 12 nm). The surface RMS is determined over the active area of the DM.

considering a two-DM set-up architecture and examining the impact of DH size.

In the following, we propose a few adjustments or improvements to equation (6) for practical reasons and to account for multiple DM situations. In practice, in equation (6) and subsequent equations, N would be better defined as the number of actuator within the LS (evaluated across its diameter). To account for the active actuators within the LS, we express ρ as the ratio of the LS and the pupil surfaces, such that

$$\rho = \frac{D_{\mathrm{LS}}}{D}, \tag{7}$$

where D is the pupil diameter and D_{LS} the LS diameter. Equation (6) then becomes

$$\mathscr{C} = \frac{16\pi}{3}\left(\frac{h_{\min}}{\rho N\lambda}\right)^2. \tag{8}$$

We note that if the LS is very aggressive, it can introduce non-linearities that might not be well captured by the former equation. Since our study employs two DMs in series, effectively doubling the total number of actuators within the LS, as a first approximation we add a factor of two in equation (8) to account for our two-DM configuration. There are likely limitations to this reasoning, and we will confront and discuss our results with this aspect in Section 4. Under these considerations, the final equation is now

$$\mathscr{C} = \frac{16\pi}{3}\left(\frac{h_{\min}}{2\rho N\lambda}\right)^2, \tag{9}$$

which can be simplified to

$$\mathscr{C} = \frac{4\pi}{3}\left(\frac{h_{\min}}{\rho N\lambda}\right)^2. \tag{10}$$

Finally, the equation can be generalized by defining γ as the number of DM used in series, so that equation (8) can be rewritten as

$$\mathscr{C} = \frac{16\pi}{3}\left(\frac{h_{\min}}{\gamma \times \rho N\lambda}\right)^2. \tag{11}$$

2.3 DM flattening maps

Flattening a DM involves adjusting its shape to eliminate low-order aberrations that may be present when the DM is not actively controlled or powered. The natural shape of DMs can exhibit significant PV and RMS variations within the active aperture. To achieve the flattest surface possible, a set of flattening voltages needs to be determined through an iterative process. The nominal voltage map represents the voltages applied to the DM to bring the surface as flat as possible, as measured by surface RMS. Typically, DM manufacturers provide a flat map with a DM at roughly 50 per cent deflection, as the flattening process reduces the stroke of the actuators available to generate the required wavefront. This map serves as a baseline or starting point for DM adjustments. It is observed that after running the EFC algorithm or similar to create the DH, the nominal voltage map may only slightly change. This emphasizes the importance of selecting the nominal voltage value for the DM offset map, as it determines the dynamic (stroke) and accuracy (minimal step size) available. The required stroke for the DM is related to the expected amplitudes of the errors the DM needs to correct in the system, and the minimal step size is crucial for achieving high-fidelity correction.

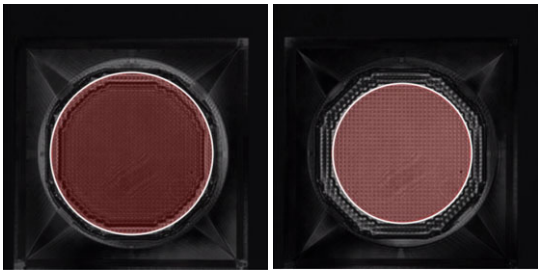

Figure 3. The image showcases a Kilo-C DM from Boston Micromachines, captured using a Zygo interferometer. The left image displays the surface of the entire reflective area with a diameter of 11.05 mm, while the right image zooms in to reveal the active area, which is restricted to 9.9 mm.

As an illustration, in Fig. 2, we present a series of flattening maps for one of the SPEED DMs (Kilo-C DM from Boston Micromachines). These maps were obtained using a FIZEAU interferometer, specifically the ZYGO Verifire XPZ from Zygo Corp, and were determined through an iterative process where an image was taken at each step using the Zygo. In Fig. 3, we illustrate the active area of the DM over which the RMS values are measured (952 actuators, white circle in the right image), while the entire reflective area is 11.05 mm (white circle in the left image). Our testing reveals that within the voltage range of 40 to 180 V, a final RMS surface quality around 10 nm over the DM's active area (9.9 mm) is achievable, regardless of the targeted voltage level (see Fig. 4). However, it is noticeable in Fig. 2 that higher voltage maps result in stronger side effects at the border of the DM's active area, with increased tension observed at the edges of the membrane. While these results are not at all presented as the upper limit of what is achievable in practice (Evans

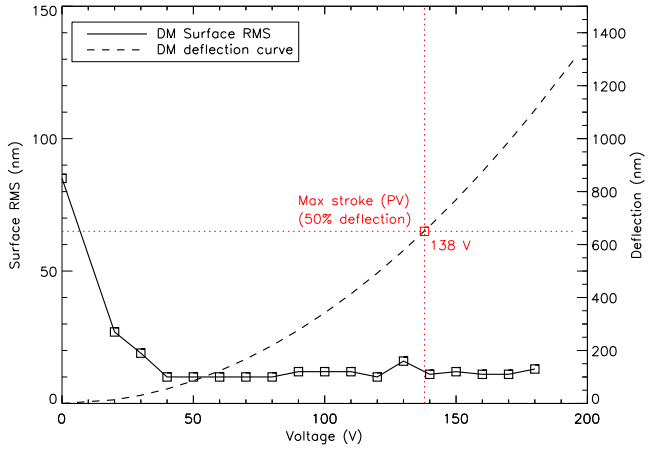

Figure 4. The RMS of the DM surface shape is plotted as a function of the voltage maps. The actuator deflection curve is included to identify the typical DM manufacturer's flat map voltage value, which is approximately at 50 per cent deflection.

et al. 2006), they provide an argument that any voltage map could, in principle, with equal surface RMS quality, be used as a starting point for generating a DH, with potential side effects particularly evident in very high-voltage cases. In low-voltage ranges, the dynamic might be insufficient to adequately flatten the DM. In our case (see Fig. 4), we cannot fairly discriminate between limitations in RMS resulting from a lack of dynamic range in the DM and limitations inherent to our process set-up. The results presented in Fig. 4 are for purely illustrative purposes.

3. NUMERICAL ASSUMPTIONS

In this section, we outline the general assumptions of our numerical modelling methodology and DH algorithm, following the same formalism as in Beaulieu et al. (2017) and Beaulieu et al. (2020).

3.1 Speckle distribution modelling

In our study, the diffraction pattern in the science image arises from (i) a segmented and obstructed pupil, which corresponds to the SPEED pupil (Martinez et al. 2023) mimicking the features of the *Extremely Large Telescope*, and (ii) an optical set-up with static aberrations. We specifically exclude quasi-static aberrations, assuming that the correction time-scale is shorter than structural or thermal changes, as well as certain sources of noise (detector noises, wavefront sensing errors, etc.). This simplification allows us to focus on specific aspects of the optical system. For simulating static aberrations, each optic is computed with random static aberrations defined by their total amount of aberration (in nanometre RMS over the optic's physical size) and their frequency distribution [power law of the power spectral density (PSD)]. We define each paraxial lens with standard optic qualities, i.e. with 5-nm RMS aberration and a power law of the PSD in f^{-3} (typical to current manufacturing errors). To ensure statistical robustness, we generate 128 phase realizations per optic. The performance is computed for each of these 128 cases. The choice of 128 realizations has been validated for statistical reliability (Beaulieu et al. 2017).

3.2 DH algorithm

Our analytical approach, based on energy minimization, determines the optimal settings for the DMs to minimize energy at the image plane, resulting in the formation of a DH. Further details about the mathematical formalism, optimization criteria, and specific considerations can be found in the literature for a more comprehensive understanding (Give'on et al. 2007; Pueyo et al. 2009; Groff 2012; Beaulieu et al. 2017).

We summarize the formalism for clarity:

(i) E_0 as the initial aberrated field with its amplitude A and its phase φ,
(ii) C_1 as the linear operator from the pupil plane (where the first DM is located) to the focal plane,
(iii) C_2 as the linear operator from the second DM (out-of-pupil plane) to the image plane,
(iv) C_{12} as the linear operator from the first to the second DM plane,
(v) a as the DMs phases coefficients, and
(vi) g and h as the influence functions of the first and second DM, respectively.

We assume that all the phases are small enough to approximate $e^{i\varphi}$ by $1 + i\varphi$, and that $C_{12}[E_0.e^{i\phi_1}]$ can be written in the form of $Ae^{i\phi}$ (and thus can be approximated by $A(1 + i\phi)$). The intensity inside the DH can be written as

$$I_{\rm DH} = {}^t a\, M_0\, a + 2\,{}^t a\, \Im(b_0) + d_0, \tag{12}$$

where $M_0 = G^* G$,

$$G = [G_1, G_2],$$

$$G_1 = \begin{bmatrix} \\ [C_1\{Ag_j\}]_i \\ \\ \end{bmatrix},$$

$$G_2 = \begin{bmatrix} \\ [C_2\{Ah_j\}]_i \\ \\ \end{bmatrix},$$

$$b_0 = \begin{bmatrix} G_1^*\, C_1\{E_0\} \\ G_2^*\, C_1\{E_0\} \end{bmatrix},$$

$$d_0 = \langle C_1\{E_0\}, C_1\{E_0\}\rangle.$$

where M_0 represents the system response to each DM poke, b_0 represents the interaction between the DM and the aberration, and d_0 is the initial intensity with aberrations and flat DMs ($a = 0$). The solution

$$a = -M_0^{-1}\Im(b_0), \tag{13}$$

that represents the DM coefficients, minimizes the energy inside the DH. Other algorithms such as EFC (Give'on et al. 2007) and the stroke minimization method (Pueyo et al. 2009) optimize the contrast ratio and limit large stroke excursion. Because our model uses monochromatic light and assumes a perfect wavefront sensor, in our analysis, we do not handle large stroke deviation.

In practice, we compute the interaction matrix M_0 by first poking each DM actuator. Subsequently, we Fresnel-propagate the wavefront from the DM to the focal plane, recording the complex amplitude assuming a perfect wavefront sensor. The optimization process involves an initial iteration to compute DM coefficients, addressing challenges posed by low singular values. Additionally, we employ an iterative process to optimize contrast, accounting for non-linearities in the optical operators. As discussed in Beaulieu et al. 2017 (see fig. 9 in that paper), empirically setting the singular value threshold

and carefully handling non-linearities contribute to achieving the best contrast in the DH region.

We use the PROPER code for Fresnel propagation between each optical element (Krist 2007). The PROPER code and the DH algorithm were originally written in IDL but translated into C++.

3.3 Nominal and alternative high-contrast imaging set-ups

End-to-end simulators play a crucial role in advancing our understanding of coronagraph instrument performance in various scenarios and for different purposes, such as technology demonstration for exoplanet missions (Krist et al. 2011), statistical analysis of budget errors or system analysis (Beaulieu et al. 2017), and assessing the impact of telescope/instrument parameters on performance (Juanola-Parramon et al. 2019). Each study addresses specific aspects and conditions relevant to its objectives, collectively contributing to the broader field of exoplanet mission planning and coronagraph optimization.

This study offers insights into the relative impact of various set-up parameters on the contrast in the DH when DM quantization errors are involved. These parameters include the optical set-up configuration (DM positioning), DM characteristics (deflection curve, flattening map, and actuator number), and DH characteristics [IWA, outer working angle (OWA), and FoV]. The comprehensive analysis covers a range of errors, providing practical considerations for realistic optical set-ups. We establish a nominal case as a basis for comparison to assess the relative impact of each parameter. This case involves a set-up with 25 optics, including (i) an obscured mask with spiders located on to a tip-tilt mirror, (ii) a perfectly co-phased segmented mirror with 163 segments, (iii) a theoretical PIAACMC coronagraph developed for SPEED (Martinez, P. et al. 2023), or alternatively, an ideal perfect coronagraph (Cavarroc et al. 2006; Sauvage et al. 2010, note that the perfect coronagraph is sensitive to aberrations and cannot correct for the phase contribution), and (iv) two DMs with 34x34 actuators, and located at 1.5 and 0.2 m from the pupil plane. When a DM is placed at the pupil plane, the beam footprint corresponds to 22x22 actuators (active actuator number at the pupil of 7.7 mm diameter). However, for out-of-pupil plane DMs, the Fresnel pattern is larger than the pupil size, and we extended the full DM range to 32x32 actuators of the 34x34 actuators available. As a consequence, unless specified otherwise, $N = 32$ in most of our simulations.

The nominal case assumes 5-nm RMS aberration with a PSD in f^{-3} for each passive optic, including the dichroic and the DMs windows. These parameters serve as the reference throughout the paper unless specified otherwise.

Given that our simulations assume a perfect wavefront sensor and exclude amplitude and temporal errors, the algorithm achieves very high contrast, surpassing what real instruments can achieve. Nevertheless, such nominal contrast ratio serves as a reference, highlighting that improperly set optical parameters can degrade the contrast level to its limiting value.

Our nominal case is versatile, allowing the optical configuration of the two DMs to be adjusted for optimal performance in various DH scenarios (Beaulieu et al. 2017). This study considers various DM optical set-ups to assess scenarios where both small and moderate angular separations in DH are targeted. For comparison purposes, the evaluation is not restricted to small angular separations. When referring to DM distances, DM_1 is consistently located upstream or in the pupil plane, while DM_2 is consistently downstream.

We consider two science DH configurations: (i) a small angular separation scenario (small IWA and OWA, and a small FoV), referred to as Case 1, with a DH ranging from $0.8\lambda/D$ to $4\lambda/D$, and (ii) a moderate angular separation situation, referred to as Case 2, with a DH ranging from $3\lambda/D$ to $7\lambda/D$. For both cases, we explore two optical configurations regarding DM positioning: Case 1A, where DM_1 is in the pupil plane and DM_2 is positioned 1500 mm downstream; Case 1B, where DM_1 is located 200 mm upstream from the pupil plane and DM_2 is positioned 1500 mm downstream; Case 2A, where DM_1 is situated 200 mm upstream from the pupil plane and DM_2 is positioned 600 mm downstream; and Case 2B, where DM_1 is located 200 mm upstream from the pupil plane and DM_2 is positioned 1000 mm downstream. While all these configurations are optimized for DH characteristics based on a former analysis (Beaulieu et al. 2017), the optical variations (A and B) in each case (Case 1 and 2) enable a thorough investigation of optical set-up dependence and potential significance in the analysis, particularly by introducing a situation where a DM is in the pupil plane (Case 1A). A summary of all these configurations is provided in Table 1.

Table 1. Configuration tested in simulation listed by names and expressed as a function of the DM positioning (DM_1 upstream of or in the pupil plane, DM_2 downstream the pupil plane) and DH configuration from small to moderate angular separations.

Configuration	$\boldsymbol{DM_1}$(mm)	$\boldsymbol{DM_2}$(mm)	DH size ($\boldsymbol{\lambda/D}$)
Case 1A	0	1500	0.8−4
Case 1B	200	1500	0.8−4
Case 2A	200	600	3−7
Case 2B	200	1000	3−7

4. NUMERICAL RESULTS

In this section, we present the results obtained from numerical simulations. The numerical pupil diameter size is 225 pixels for a grid size of 1024 pixels. The simulation is monochromatic, with a wavelength of 1.65 µm. Our performance criterion is defined as the 5σ contrast ratio histogram computed for each of the 128 random realizations. It represents the number of random realizations that achieve a given contrast ratio inside the defined DH.

We present our results in two forms: histograms, as previously discussed and used in Section 4.1, and as the median contrast of histograms, as used in Section 4.2. Section 4.1 addresses the impact of the DM flattening maps, where results in the form of histograms are relevant to highlight dispersion in the contrast as a function of phase realization, providing a statistical approach to assess the ability to sustain the contrast. On the other hand, Section 4.2 addresses the impact of the stroke precision, where trends are sought, and a statistical approach is less relevant than a unique contrast estimate defined as the median of the histogram of the 128 random realizations.

In our simulation, as discussed and demonstrated in the lab (see Section 2.3), the flattening maps of our DM ensure consistent RMS surface quality regardless of the voltage applied to the map. The results presented in Section 2.3 were not intended to represent the maximum achievable performance in practice. Therefore, we designed our DM flattening maps to exhibit 5-nm RMS aberration, consistent with passive optics as discussed in the previous section.

4.1 Impact of the DM flattening maps

We first consider our nominal case, as defined in Beaulieu et al. (2020), where DM positioning is optimized for a DH ranging from

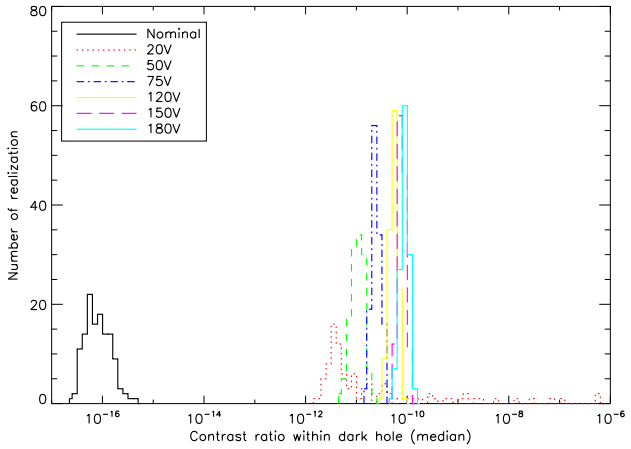

Figure 5. 5σ contrast ratio histogram for DH from $0.8\lambda/D$ to $4\lambda/D$, assuming DM_1 at 200 mm and DM_2 at 1500 nm (Case 1A), as a function of various flattening voltage maps. The nominal case corresponds to no stroke limitation imposed by the flattening map. Simulation assumes a perfect coronagraph.

$0.8\lambda/D$ to $4\lambda/D$, dedicated to small angular separations and FoV (Case 1B, DM_1 at 200 mm and DM_2 at 1500 nm), and in this case, the coronagraph is a perfect coronagraph.

In this configuration, we can assess the limitation imposed by the stroke limitation originating from the voltage of the DM flattening map around which the DH is started and is evolving, with no impact from the coronagraph (ideal case). The results of the simulation, exploring the impact of flattening map voltage values ranging from 20 to 180 V, on the contrast in the DH, are presented in Fig. 5. Fig. 5 shows following points: (i) The lower the voltage of the flattening map, the better the results, which points out the interest of low voltages in allowing higher DM step resolution; (ii) independently from the value of the voltage of the DM flattening map, departing from the ideal and nominal case with no stroke limitation does impact the contrast on the DH (the nominal case, black line, leads to non-realistic contrast values); and (iii) the dispersion, as seen in the 20-V case (red histogram), indicates that at very low voltage, because the stroke dynamic is severely reduced, the probability of obtaining deep contrast is also reduced.

In Fig. 6, similar results are presented but extended to all the DM set-up scenarios and DH sizes, as discussed in the previous section and summarized in Table 1 (Case 1A and B, Case 2A and B), and when the coronagraph is a PIAACMC from the SPEED testbed. In these cases, the nominal scenario without stroke limitation is omitted from presentation, as it consistently results in non-realistic contrast values, as illustrated in Fig. 5 (black histogram), ranging from 10^{-13} to 10^{-14}. The trend is similar, independently from the DH and DM configurations, and highlights that, in contrast to what the manufacturer provides (flattening map at 50 per cent deflection), low-voltage maps are preferable, DH-wise. The coronagraph type does not either impact the results [perfect coronagraph (see Fig. 5) and PIAACMC (see Fig. 6)].

4.2 Impact of the stroke precision

In this part, we assess the impact of DM stroke precision on the contrast in the DH. The algorithm used for the DH is described in Beaulieu et al. (2020) and has been adapted to consider the smallest step an actuator can achieve by taking into account the quadratic power law of the actuator deflection curve, as well as the voltage of the flattening map from which the DH is initiated. For simplicity, it is assumed in the subsequent analysis that the stroke precision value is the same for each actuator of the two DMs. In this section, special attention is given to comparing simulation results with predictions derived from equation (11). In equation (11), the parameters used are $N = 32$, $\lambda = 1.65$ µm, and $\gamma = 2$ in all cases, with $\rho = 1$ and $\rho = 0.8$ when a perfect coronagraph and PIAACMC are considered, respectively. The value of $\rho = 0.8$ for the PIAACMC has been evaluated by considering the impact of the PIAACMC LS on the geometrically redistributed pupil from the PIAA stage.

A first step in our analysis focuses on predictions from equation (11) when a perfect coronagraph is considered and comparing a uniform with a quadratic power law for the actuator deflection curve. The uniform case corresponds to a situation where the motion is proportional to the voltage with uniform precision regardless of the applied voltage. This step is useful as a comparison basis to assess the impact of the actuator deflection curve power law on equation (11). Fig. 7 (left image) shows the contrast (median) in the DH as a function of the stroke precision in nanometre for a perfect coronagraph and a uniform case (black diamonds) or a quadratic actuator deflection curve (red asterisks). Predictions from equation (11) are shown in a solid black line. It is readily observable that when a uniform precision is considered, the match between simulations and predictions is fairly good in both trend and in contrast level. When a quadratic power law is considered, while the trend is similar to the prediction given by equation (11) in mid- and high-level voltage ranges, a discrepancy is observable in the low-voltage range, below $\sim$50 V. This behaviour will be more visible in the results presented in Fig. 7 (right image).

In Fig. 7 (right image), we present the same analysis but with a PIAACMC instead of a perfect coronagraph, a quadratic actuator deflection curve only, and for multiple DH and DM configurations as presented in Table 1. Again, the trend of the contrast derived from simulations (asterisks, diamonds, triangles, and squares) is similar to the prediction given by equation (11) in mid- and high-level voltage ranges with a limited mismatch in terms of contrast level (see Table 2 for a quantitative evaluation restricted to Case 1B and 2A that are representative as upper and lower limits in the discrepancy/dispersion), and a discrepancy is observable in the low-voltage range. The discrepancy shows significant dispersion in the contrast levels. Comparing these results (Fig. 7, right image) with the previous ones (Fig. 7, left image) demonstrates that the mismatch with equation (11) in the low-voltage regime occurs independently from the coronagraph type (perfect coronagraph or PIAACMC). In the low-voltage domain, because the resolution gets higher, the dynamic is lower, which might explain the discrepancy as well as the dispersion in the contrast for various configurations. When the quadratic power law is considered for the actuator deflection curve, it induces a dependence on the minimal resolution step of an actuator to the voltage, while the uniform precision case is free from this dependence. We note that the stroke levels on both DMs at the end of the correction process to achieve the DH never evolve significantly or exhibit abnormal state, which cannot explain the observed phenomenon. In the almost middle range regime of the quadratic power law (mid-voltage range), the discrepancy is minimal and can be as low as a factor of 1.2 (see Table 2, where $\mathscr{R}$ stands for the ratio of the contrast evaluated in simulation to that of the contrast derived from equation 11), and the trend predicted by equation (11) is respected. In the high-voltage domain, this behaviour is consistent. However, in this regime, and because our simulations do not account for side effects at the border of the DM's active area, with increased tension applied at the edges of the membrane, we expect that dispersion should appear.

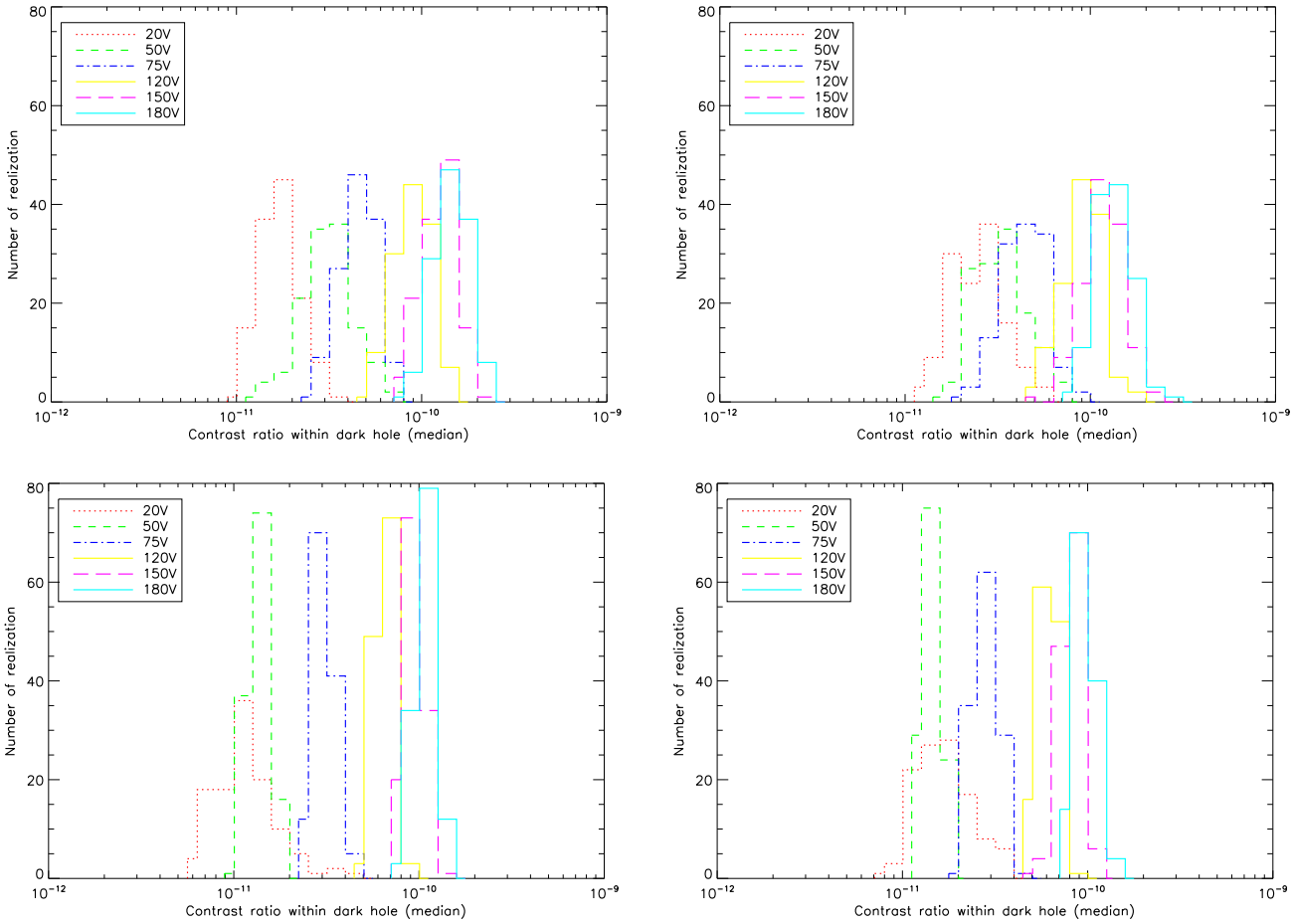

Figure 6. 5σ contrast ratio histogram as a function of various flattening voltage maps for Case 1A (top-left image), Case 1B (top-right image), Case 2A (bottom-left image), and Case 2B (bottom-right image). The nominal case corresponds to no stroke limitation imposed by the flattening map. Simulations assume the SPEED PIAACMC.

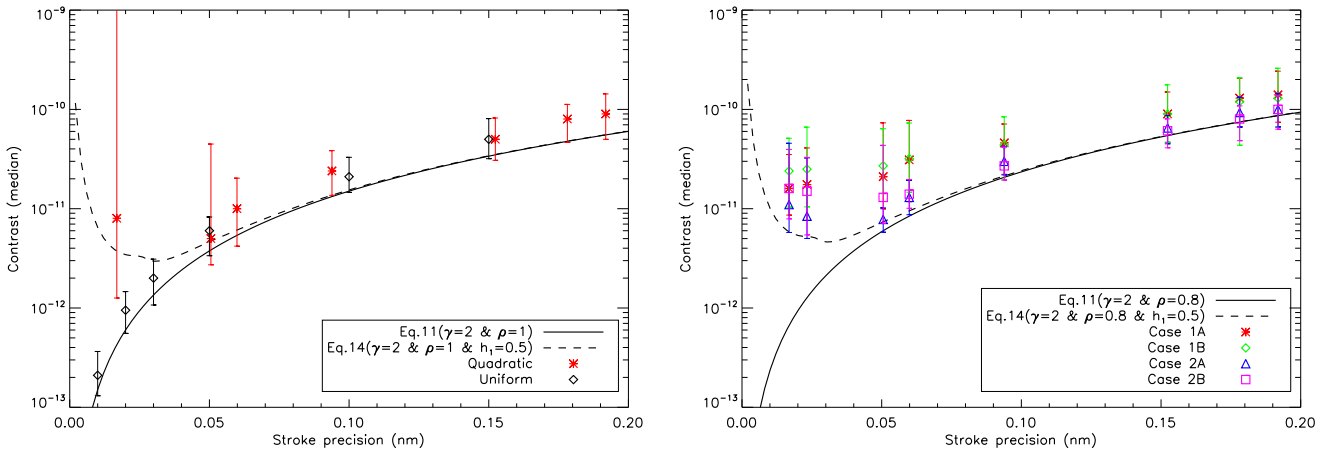

Figure 7. The left image shows the contrast (median of histograms) in the DH as a function of the stroke precision in nanometre for a perfect coronagraph and a uniform precision law. The right image shows the same for a PIAACMC and a quadratic actuator deflection curve. The simulation results (asterisks) are compared with predictions from equation (11) (full line) with $\rho = 1$ and $\gamma = 2$ (left image) and with $\rho = 0.8$ and $\gamma = 2$ (right image). The error bars represent the minimum and maximum contrast values achieved in the corresponding histogram.

Table 2. Summary of contrast (median of histograms) values obtained in the DH (PIAACMC and quadratic power-law actuator deflection curve) as a function of the stroke precision in nanometre (or initial DM flattening map voltages in V) for cases 1B and 2A, compared with prediction derived from equation (11).

Voltage (V)	20	25	30	50	75	120	150	180
$h_{\min}$(nm)	0.016	0.023	0.050	0.060	0.094	0.152	0.178	0.192
$\mathscr{C}$(equation 11)	6.6×10^{-13}	1.2×10^{-12}	5.9×10^{-12}	8.4×10^{-12}	2×10^{-11}	5.4×10^{-11}	7.5×10^{-11}	8.6×10^{-11}
				Case 1B				
$\mathscr{C}$(simulation)	2.4×10^{-11}	2.5×10^{-11}	2.7×10^{-11}	3.2×10^{-11}	4.4×10^{-11}	9×10^{-11}	1.2×10^{-10}	1.3×10^{-10}
$\mathscr{R}$	36	20.8	4.6	3.8	2.2	1.6	1.6	1.5
				Case 2A				
$\mathscr{C}$(simulation)	1.1×10^{-11}	8.4×10^{-12}	7.8×10^{-12}	1.3×10^{-11}	3×10^{-11}	6.5×10^{-11}	9.3×10^{-11}	1.0×10^{-10}
$\mathscr{R}$	16	7	1.3	1.5	1.5	1.2	1.2	1.2

Regarding our various DH and DM configurations, we notice that, as presented in Fig. 7 (right image), the results are fairly similar, which further confirms that the DM positioning resulting from a former analysis (as a function of the DH size, IWA, and OWA) is correct. We remind the reader that, complying with the specifications of a given test-bed or instrument (FoV, targeted contrast, optics propagation distances, aberration types, etc.), Beaulieu et al. (2017, 2020) have demonstrated that the optimal distances of the DMs relative to the pupil plane are crucial and can be optimized. In other words, the condition for the location of the DMs is driven by the ability of the DMs to get a balanced efficiency of correction over the frequency range of the DH. Fig. 7 (right image) thus indicates that the comparison of simulation results to equation (11) is independent of the DH size and DM cases considered to a small coefficient. We can conclude that equation (11) captures the impact of DM quantization errors on the contrast in the DH similarly when small angular separations or moderate angular separations are targeted.

We note that equation (11) always provides a best case contrast limit in the DH compared with simulations, which is reassuring. We see two potential error sources that could explain the difference in contrast levels between our simulations and predictions from equation (11), even if limited in the mid-voltage regime: (i) Because our DMs are almost never in a pupil plane, it is questionable whether considering that $\gamma = 2$ fairly describes the number of actuators in the LS. While there are effectively two DMs in series and $2 \times N$ actuators in the LS, because DMs are out-of-pupil planes in most of the cases studied, the number of *fully efficient* actuators in the LS might be lower when considering this parameter in equation (11). Since the positioning of DMs varied from configuration to configuration, it is challenging to define and optimize a parameter to account for this effect. (ii) In order to add the continuous membrane of the DM to our code, we treat our DM surface in simulation as a linear superposition of actuators with an influence function using a Gaussian-shaped fitting model, but equation (11) does not account for that. These aspects (i) and (ii) (see the study described in Ruane et al. 2020, where the authors take into account the DM actuator shape) degrade the contrast predicted in the DH by equation (11).

In the low-voltage regime, where the most significant deviation between simulation and prediction occurs, the situation cannot be explained by the two aspects discussed previously. This rather suggests that a lack of actuator stroke, rather than precision, is at work. In fact, equation (11) does not account for the available actuator stroke, which depends on the voltages applied to the DMs to make the surface as flat as possible before DH generation. At low voltages, as seen in Figs 1 and 4, below approximately 20 per cent of the maximum deflection (depending on whether we consider a single actuator deflection curve or, for instance, a 4x4 actuators region deflection curve), a MEMS DM system is dominated by its quadratic relationship regime between deflection and the voltage applied, while from 20 per cent to 90 per cent of the maximum deflection, it has a nearly linear relationship. Below 20 per cent, as the voltage decreases, the available stroke becomes increasingly limited. Moreover, predictions provided by equation (11), when stroke precision tends towards infinitely small precision, does not capture reality in the case of MEMS DMs. It tends towards infinite contrast levels, whereas the DM's stroke range should tend towards zero, as should the contrast. Therefore, extending the analytic model provided by equation (11) to account for this discrepancy is necessary. Further, it is worth noting that equation (11) is based on statistical and modal arguments, relying on the hypothesis that the peaks and valleys of the ripple have values $\pm h_0$ (see Appendix A). In the low-voltage regime, the PV symmetry of h_0 might no longer be valid.

To capture the deviation from the pure power law in the low-voltage regime, we introduce an additional parameter, denoted as h_1 in equation (11), balanced by a gain function (g). The gain function g (i) ensures that the correction applied by the term h_1 is not constant but evolves with the value of $h_{\min}$, thus depends on the voltage for MEMS DMs, and (ii) describes the asymptotic behaviour of the contrast in the DH for infinitively small stroke precisions. This ensures it has a strong impact at very low voltages, with decreasing impact as the voltage increases, and limited or no impact at mid and high voltages. With these considerations, equation (11), can be written as

$$\mathscr{C} = \frac{16\pi}{3}\left(\frac{h_{\min} + h_1 \times g}{\gamma \times \rho N \lambda}\right)^2, \tag{14}$$

where the gain function g is expressed as $g = \frac{1}{\delta}$, and is defined as the inverse of the deflection function curve (see Fig. 1 or 4, that shows δ as a function of the voltage for our Kilo-C DMs), so that the correction is balanced by capturing the stroke dynamic limitation behaviour (g tends towards infinity at low values, and tends towards zero at high values). Equation (11) corresponds to $h_1 = 0$ nm. The correction proposed in equation (14), using $h_1 = 0.5$ nm, empirically determined so that the contrast floor nature of the equation is preserved, can be compared with equation (11) in Fig. 7 (left and right images) and is presented as a dashed black line. Fig. 7 shows that when equation (14) is considered, (i) the discrepancy in the low-voltage regime is reduced to reasonable values, (ii) the behaviour when the stroke precision tends towards zero is accounted for, and (iii) predictions from equation (11) in the mid- and high-voltage domains are respected. We note that the sampling of the curve

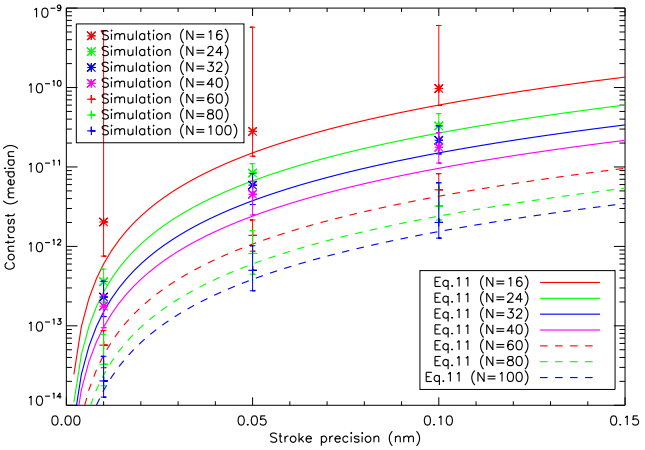

Figure 8. Contrast (median of histograms) in the DH as a function of the stroke precision in nanometre for various actuator numbers (N) in the case of a perfect coronagraph and a uniform stroke precision law. The simulation results (asterisks) are compared with predictions from equation (11) (full line) with $\rho = 1$ and $\gamma = 2$. The error bars represent the minimum and maximum contrast values achieved in the corresponding histogram.

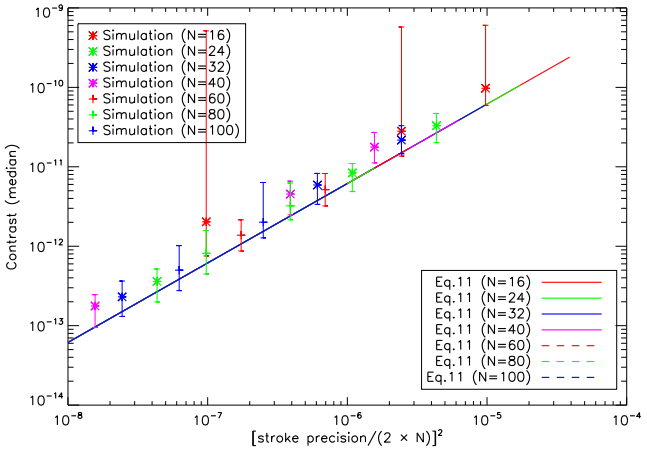

Figure 9. Same data sets and conditions as in Fig. 8, but now the contrast (median of histograms) in the DH is expressed as a function of the square of the stroke precision divided by the number of actuators ($2 \times N$) considered. The error bars represent the minimum and maximum contrast values achieved in the corresponding histogram.

representing equation (14) in Fig. 7 is not as good as that of equation (11) due to the gain function, which uses the deflection curve of our mirrors as provided by the manufacturer (see Fig. 1) and whose sampling is much poorer.

To generate the sinusoidal signals corresponding to the frequencies needed for DH, both high and low voltages are required (in the sense of peak and valley values). In the regime where the DM system is dominated by its quadratic law, good precision is achievable at the minimum values of a given sinusoid, but the maximum values are less precise. In addition, the available stroke disrupts the expected symmetric actions capability of the mirror on the peak and valley values. This leads to slower and less accurate convergence, as shown in Fig. 7. If there are fewer aberrations to correct, the impact of the function g should be less significant. Conversely, the effect can be much stronger when correcting significant aberrations. This discrepancy is not captured by the gain function itself but is by the empirical adjustment using the h_1 parameter.

4.3 Impact of the actuator number

In this section, we compare the contrast obtained in the DH when the number of DM actuators (N) is changed to predictions from equation (11). Since we observed that predictions from equation (11) are independent of the DH size and DM configuration (DM positioning), we restrict our analysis to Case 1B. For the same reason, we consider a perfect coronagraph ($\rho = 1$) and a uniform step accuracy for the actuator deflection curve to eliminate the discrepancy and dispersion at low voltages. The goal is to isolate the effect of N between simulations and predictions ($\gamma = 2$). In these conditions, we consider various N values to widely explore this parameter space: 16, 24, 32, 40, 60, 80, and 100, and the results are presented in Fig. 8, where the contrast in the DH obtained from simulations is represented either by asterisks or plus signs, while predictions derived from equation (11) are shown as solid and dashed lines. We remind the reader that due to the Nyquist criterion, the number of actuators N limits a DM's overall performance: It can correct up to a radius of $\frac{\lambda N}{2D}$ at the image plane. Restricting the analysis to Case 1B (small FoV and IWA DH) helps guarantee that for most of N values considered, the size of the DH is lower than the DM's correction area. This ensures that aliased speckles caused by a speckle whose central frequency is outside the DH but within the correction area can be mitigated. We note that for $N = 16$ (cutoff frequency of $8\lambda/D$ aliased speckles might still have an effect) DH OWA is $4\lambda/D$.

Fig. 8 displays the contrast (median) in the DH as a function of the stroke precision in nanometre and the number of actuators (N). The blue curve and asterisks are similar to the results presented earlier in Fig. 7 (left image). For all N values, equation (11) consistently predicts slightly better contrast than the values obtained in simulations. The origin of the discrepancy might be explained similarly to the previous subsection (see Section 4.2). It is noteworthy that despite the limited discrepancy with predictions from equation (11), the trend in the dependence of the contrast in the DH on N obtained from simulations is similar and is fairly captured by equation (11). Furthermore, the number of actuators also impacts high-contrast imaging within the DM correction range: Performance depends on the DM's capability to accurately reproduce a phase pattern, even for spatial frequencies less than $\frac{\lambda N}{2D}$, and equation (11) might not be able to account for that. This could explain why the dispersion around the contrast value (median) represented with error bars is significant for $N = 16$, along with the potential impact of aliased speckles (as already discussed).

Fig. 8 also suggests that smaller errors in actuator stroke is nearly equivalent to increasing the number of actuators: For instance at 0.05-nm stroke precision, $N = 24$ provides better contrast level than $N = 40$ at stroke precision of 0.1 nm. Similarly, at 0.05-nm stroke precision, $N = 60$ provides better contrast level than $N = 100$ at stroke precision of 0.1 nm. In other words, improving the stroke accuracy of a factor of 2 is nearly equivalent at doubling the number of actuator.

Fig. 9 shows similar results as in Fig. 8, but this time it provides the contrast as a function of the square of the stroke precision divided by the number of actuators. It further illustrates the proximity between simulation results and predictions derived from equation (11).

5. CONCLUSIONS

In our study, we investigate the dependence of MEMS DM quantization errors and initial voltage maps on small to moderate angular separation DHs. We compare our results with predictions generated

by a simple and widely used formula proposed by several authors (Trauger et al. 2007, 2011; Traub & Oppenheimer 2010; Ruane et al. 2020).

A by-product of our study is to determine the domain of validity for equation (11) in expressing the relationship between DM quantization error and DH image quality. This investigation specifically focuses on scenarios where (i) DMs are used in series, (ii) a quadratic power law defines the actuator deflection curve, and (iii) small angular separations are targeted. The examination of the impact of the initial voltage value of the DM flattening maps serves as a complementary aspect of the study. It is essential to emphasize that equation (11) was originally formulated without incorporating factors such as DH size, multiple DM architecture, out-of-pupil plane DM configuration, and irrespective of specific science objectives, such as small FoV/IWA DH or wider FoV/IWA DH. Our study provides insights into these aspects. The domain of validity of this formula is thoroughly studied, and the formula is subsequently extended to the case of a multi-DM architecture and to the case of a quadratic relationship between the voltage applied to an actuator and its corresponding deflection.

We demonstrate that the contrast limit in the DH due to DM quantization, as predicted by equation (11), is generally valid when a uniform stroke precision is sought. However, a discrepancy and dispersion are observed at the low-voltage regime for a quadratic power law. In the case of the manufacturer's quadratic power law, equation (11) is found to be valid in the mid-voltage range but inefficient in accurately predicting contrast in the low-voltage range and potentially in the high-voltage regime. Notably, the results are independent of the coronagraph type, DH size, or DM configuration, with no observed dichotomy between small and moderate angular separation science cases. It is essential to recognize that equation (11) consistently provides a best-case contrast limit in the DH, offering a reference frame for assessing the relevance of contrast results. Nevertheless, fine-tuning predictions based on equation (11) or its extended version (equation 14) is a challenging and likely futile task due to various factors, such as actuator stability, hysteresis, inter-actuator influence, etc., which are difficult to predict accurately for each actuator in a DM.

When it comes to DM flattening map voltages, using the manufacturer flattening map defined at roughly 50 per cent deflection is not optimal in terms of DH performance. Lower voltage values are preferable, as they increase the DM minimal resolution step and, consequently, the accuracy. However, we also demonstrate that in the low-voltage domain, the risk of divergence in the DH algorithm increases certainly due to a lack of dynamic range. To account for this effect, we extend the analytic model proposed by equation (11) by incorporating a correction term as expressed in equation (14), which captures the actuator stroke range with voltages.

Beyond the challenge of achieving and assessing the impact of the minimal step, the stroke error (the difference between the specified and the real actuator position) is critical and largely dependent on the variation in the maximum range of the amplifiers in the electronics. This leads to different amounts of error at different points on the actuator deflection curve. Actuator stability (the ability of the actuators to hold their shape over time) and repeatability (the ability of the actuator to return to the same position under the same applied voltage consistently) are also crucial factors but are beyond the scope of this study (Evans et al. 2006). Additionally, the continuous phase-sheet MEMS DM stroke depends on the displacement of adjacent actuators (Bifano et al. 2010), necessitating a conservative margin to be applied to equation (11), as discussed in Ruane et al. (2020).

Finally, while the most important DM properties for high-contrast imaging are the number of actuators, the surface height resolution, and the stability/repeatability of the mirror surface, we show that smaller errors in actuator stroke is nearly equivalent to increasing the number of actuators, if one disregards FoV considerations (IWA and OWA are defined by the number of actuators). Because it might be simpler to enhance the precision of existing mirrors through DM controller developments than to create new high-density actuator DMs, this result could have implications for technological developments for future projects (e.g. the Habitable World Observatory; Vaughan et al. 2023), though a trade-off must be explored between contrast and FoV in the DH.

ACKNOWLEDGEMENT

The authors are grateful to the OPAL infrastructure from Observatoire de la Côte d'Azur (CRIMSON) for providing resources and support.

DATA AVAILABILITY

The data underlying this article will be shared on reasonable request to the corresponding author.

REFERENCES

Ahn K. et al., 2023, A&A, 673, A29
Beaulieu M., Abe L., Martinez P., Baudoz P., Gouvret C., Vakili F., 2017, MNRAS, 469, 218
Beaulieu M., Martinez P., Abe L., Gouvret C., Baudoz P., Galicher R., 2020, MNRAS, 498, 3914
Belikov R. et al., 2010, American Astronomical Society Meeting Abstracts, #215, 1127
Bendek E., Ruane G., Prada C. M., Mendillo C. B., Riggs A. J. E., Serabyn E., 2020, J. Astron. Telesc. Instrum. Syst., 6, 045001
Bierden P., Cornelissen S., Lam C., Bifano T., 2011, Second International Conference on Adaptive Optics for Extremely Large Telescopes. AO for ELT 2, Victoria, BC, Canada, p. 34
Bierden P., Cornelissen S., Ryan P., 2014, American Astronomical Society Meeting Abstracts, #223, 344.03
Bifano T., Cornelissen S., Bierden P., 2010, in Clénet Y., Conan J.-M., Fusco Th., Rousset G., eds, Proc. 1st AO4ELT Conf., Adaptative Optics for Extremely Large Telescopes. EDP Sciences, France, p. 06003
Cavarroc C., Boccaletti A., Baudoz P., Fusco T., Rouan D., 2006, in Whitelock P., Dennefeld M., Leibundgut B., eds, Proc. IAU Symp. 232, The Scientific Requirements for Extremely Large Telescopes. Cambridge Univ. Press, Cambridge, p. 334
Delorme J. R. et al., 2016, A&A, 592, A119
Evans J. W., Macintosh B., Poyneer L., Morzinski K., Severson S., Dillon D., Gavel D., Reza L., 2006, Opt. Express, 14, 5558
Galicher R. et al., 2014, Proc. SPIE Conf. Ser. Vol. 9143, Space Telescopes and Instrumentation 2014: Optical, Infrared, and Millimeter Wave. SPIE, Bellingham, p. 91435A
Give'on A., Kern B., Shaklan S., Moody D. C., Pueyo L., 2007, in Tyson R. K., Lloyd-Hart M., eds, Proc. SPIE Conf. Ser. Vol. 6691, Astronomical Adaptive Optics Systems and Applications III. SPIE, Bellingham, p. 66910A
Groff T. D., 2012, PhD thesis, Princeton Univ.
Guyon O., Pluzhnik E., Martinache F., Totems J., Tanaka S., Matsuo T., Blain C., Belikov R., 2010, PASP, 122, 71
Haffert S. Y. et al., 2023, A&A, 673, A28
Juanola-Parramon R., Zimmerman N. T., Groff T., Pueyo L., Rizzo M., Bolcar M., Roberge A., 2019, American Astronomical Society Meeting Abstracts, #233, 148.06

Kay J. D., Pueyo L. A., Kasdin N. J., 2009, Proc. SPIE Conf. Ser. Vol. 7209, MEMS Adaptive Optics III. SPIE, Bellingham, p. 72090G
Krist J. E., 2007, in Kahan M. A., ed., Proc. SPIE Conf. Ser. Vol. 6675, Optical Modeling and Performance Predictions III. SPIE, Bellingham, p. 66750P
Krist J. E., Belikov R., Pueyo L., Mawet D. P., Moody D., Trauger J. T., Shaklan S. B., 2011, Proc. SPIE Conf. Ser. Vol. 8151, Techniques and Instrumentation for Detection of Exoplanets V. SPIE, Bellingham, p. 81510E
McCrea W. H., Whipple F. J. W., 1940, Proc. R. Soc. Edinburgh, 60, 281
Martinez P. et al., 2023, A&A, 680, A6
Martinez P. et al., 2014, Proc. SPIE Conf. Ser. Vol. 9145, Ground-based and Airborne Telescopes V. SPIE, Bellingham, 91454E
Martinez P., Beaulieu M., Gouvret C., Spang A., Marcotto A., 2023, The Messenger, 190, 55
Mazoyer J., Baudoz P., Galicher R., Rousset G., 2014, A&A, 564, L1
Morgan R. E. et al., 2019, Micromachines, 10, 366
Morzinski K. M., Evans J. W., Severson S., Macintosh B., Dillon D., Gavel D., Max C., Palmer D., 2006, in Ellerbroek B. L., Calia D. B., eds, Proc. SPIE Conf. Ser. Vol. 6272, Advances in Adaptive Optics II. SPIE, Bellingham, p. 627221
Morzinski K. M., Gavel D. T., Norton A. P., Dillon D. R., Reinig M. R., 2008, in Olivier S. S., Bifano T. G., Kubby J. A., eds, Proc. SPIE Conf. Ser. Vol. 6888, MEMS Adaptive Optics II. SPIE, Bellingham, p. 68880S
N'Diaye M. et al., 2013, Proc. SPIE Conf. Ser. Vol. 8864, Techniques and Instrumentation for Detection of Exoplanets VI. SPIE, Bellingham, p. 88641K
Pueyo L., Kay J., Kasdin N. J., Groff T., McElwain M., Give'on A., Belikov R., 2009, Appl. Opt., 48, 6296
Pueyo L., Kay J., Kasdin N. J., Groff T., Mc Elwain M., Give'on A., Belikov R., 2011, preprint (arXiv:1111.5111)
Riggs A. J. E., Groff T. D., Carlotti A., Kasdin N. J., Cady E. J., Kern B. D., Kuhnert A., 2013, Proc. SPIE Conf. Ser. Vol. 8864, Techniques and Instrumentation for Detection of Exoplanets VI. SPIE, Bellingham, p. 88640T
Ruane G. et al., 2020, J. Astron. Telesc. Instrum. Syst., 6, 045002
Sauvage J.-F., Mugnier L. M., Rousset G., Fusco T., 2010, J. Opt. Soc. Am. A, 27, A157
Traub W. A., Oppenheimer B. R., 2010, in Seager S., ed., Exoplanets. Univ. Arizona Press, Tucson, p. 111
Trauger J. T., Traub W. A., 2007, Nature, 446, 771
Trauger J. et al., 2007, in Coulter D. R., ed., Proc. SPIE Conf. Ser. Vol. 6693, Techniques and Instrumentation for Detection of Exoplanets III. SPIE, Bellingham, p. 66930X
Trauger J., Moody D., Gordon B., Krist J., Mawet D., 2011, Proc. SPIE Conf. Ser. Vol. 8151, Techniques and Instrumentation for Detection of Exoplanets V. SPIE, Bellingham, p. 81510G
Vaughan S. R. et al., 2023, MNRAS, 524, 5477

APPENDIX A: CONTRAST IN A DH

In this appendix, we provide a justification to equation (6) following the formalism and explanations provided in Trauger et al. (2007, 2011) and Traub & Oppenheimer (2010). In particular, this appendix is broadly inspired from the stellar intensity description in the presence of a coronagraph, and the formalism on the controlling of scattered light with DMs as proposed in Traub & Oppenheimer (2010). We thus follow the same formalism and these details are presented here for pedagogical reasons and because they are considered as a basis for our work.

Let us consider that $E_{\rm p}(u)$ represents the amplitude of the electric field in a one-dimensional telescope model of diameter D, with range $u = (-D/2, +D/2)$:

$$E_{\rm p}(u) = A(u)\exp^{i\phi(u)}. \tag{A1}$$

By Fourier analysis, the phase $\phi(u)$ can be written as the sum of many sinusoidal ripples (a disturbed wavefront across a pupil can be represented by a sum of sine and cosine). If we suppose a typical ripple that has spatial period u_0, the phase of the wavefront can be written

$$\phi_0(u) = a\cos(2\pi u/u_0 + \alpha) + ib\cos(2\pi u/u_0 + \beta), \tag{A2}$$

where the imaginary part represents the spatial variation of amplitude and the real part the spatial-variation of phase. Assuming that the peaks and valleys of the ripple have values $\pm h_0$, then the corresponding amplitude of phase delay is

$$a = 2\pi h_0/\lambda. \tag{A3}$$

In the focal plane, the complex amplitude, denoted as $E_{\rm f}$, is

$$E_{\rm f}(\theta) \approx \int_D \exp^{i\phi_0(u)} \cdot \exp^{-\frac{i2\pi\theta u}{\lambda}} {\rm d}u, \tag{A4}$$

where θ is the radial angle from the optical axis. In the small aberrations regime where $\phi(u) << 1$, the exponential can be expanded giving $E_{\rm p}(u) \approx A(u) \times (1 + \phi(u))$,

$$E_{\rm f}(\theta) \approx \int_D [1 + i(a\cos(2\pi u/u_0 + \alpha) + ib\cos(2\pi u/u_0 + \beta))] \cdot \exp^{-\frac{i2\pi\theta u}{\lambda}} {\rm d}u. \tag{A5}$$

By replacing $\cos(z)$ with $(\exp iz + \exp -iz)/2$, each term can be integrated. Defining the well-known diffracted amplitude of a single star as

$$E_0(\theta) = \frac{\sin(\pi\theta D/\lambda)}{\pi\theta D/\lambda}, \tag{A6}$$

we obtain that the diffracted amplitude is the sum of a main peak, at the expected $\theta = 0$ position of the star, plus two smaller peaks, one on each side, at $\theta_s = \pm\lambda/u_0$, where

$$E_{\rm f}(\theta) \approx E_0(\theta) + 1/2\left(ia\exp^{i\alpha} - b\exp^{i\beta}\right)E_0(\theta + \lambda/u_0) + 1/2\left(ia\exp^{-i\alpha} - b\exp^{-i\beta}\right)E_0(\theta - \lambda/u_0). \tag{A7}$$

The final intensity $I_{\rm F}(\theta) = \mid E_{\rm f}(\theta) \mid^2$ has six terms:

$$I_{\rm F}(\theta) = I_0 + I_{-1} + I_{+1} + I_{-2} + I_{+2} + I_3. \tag{A8}$$

In the last equation, I_0 is the main peak, the central star image. The next two terms are symmetrically placed speckles where

$$I_{\pm1} = 1/4\left[a^2 + b^2 \pm 2ab\sin(\alpha - \beta)\right]I_0(\theta \pm \lambda/x_0). \tag{A9}$$

Their intensities are equal only if either phase errors or amplitude errors dominate. If there is a mixture of these errors, the intensities can be unequal. These intensity variations have the same shape as translated copies of the central peak but are scaled down. The next two terms correspond to pinned speckles, which are located at the same positions as the ordinary speckles but are scaled by the local intensity of the diffraction pattern from the main peak, being anchored to the pre-existing diffraction rings (amplified by the coherent part of the wave). The last term, I_3, is negligible and omitted as it represents a cross product of the two speckles.

When it comes to intensity in a DH, speckles are, to some extent, suppressed by a DM. In the following, dynamic and quasi-static aberrations are omitted: Atmospheric errors are considered perfectly corrected by an upstream extreme adaptive optics system, and the correction time-scale involved in the DH generation is considered shorter than structural or thermal changes. Under these circumstances, we restrict our analysis to speckles described by equation (A9).

In the following, we assume that the DM is an $N \times N$ square array of actuators placed in a pupil plane. The telescope pupil is considered mapped on to the square DM by perfectly filling it, so that the ratio of the pupil surface

$$S_{\rm p} = \pi \left(\frac{N}{2}\right)^2, \tag{A10}$$

assuming N actuators per diameter, by the DM square array surface

$$S_{\rm dm} = N^2, \tag{A11}$$

is $\frac{\pi}{4}$. Assuming that the DM can fit up to about $\frac{N}{2}$ periods of a wave with N actuators in one dimension, so $\frac{N}{2}$ waves per diameter, and thus $\left(\frac{N}{2}\right)^2$ in two dimensions. By analogy, it is assumed that there are as much as M modes in the full area of the pupil that the DM can control, considering the active actuators over the pupil footprint only, so that

$$M = \frac{\pi}{4}\left(\frac{N}{2}\right)^2. \tag{A12}$$

By considering a unique mode of averaged amplitude h_0, the speckle produced by this mode has relative intensity of $a^2/4$ by considering results from equation (A9):

$$I_{\pm 1}/I_0 = a^2/4. \tag{A13}$$

Using the results given by equation (A3), we finally obtain

$$I_{\pm 1}/I_0 = (\pi h_0/\lambda)^2. \tag{A14}$$

Summing the contribution of multiple modes with random phases (equivalent to summing M complex vectors of average length h_0 but with random phases) and by using the analogy and the well-known result from the random walk problem in two dimensions (which considers a sum of M two-dimensional vectors with random orientations, the RMS distance after M unit steps of length l is given by $d_{\rm rms} = l \times M^{1/2}$; McCrea & Whipple 1940), we can express the RMS surface error in the DM actuator settings, denoted as $h_{\rm rms}$, from the average amplitude, where

$$h_{\rm rms} \approx h_0 \times M^{1/2}, \tag{A15}$$

where it can be rewritten as

$$h_{\rm rms} = \frac{\sqrt{\pi} N h_0}{4}. \tag{A16}$$

Because the DM is a reflective device, it must be controlled to a surface error of $h_{\rm rms}/2$ in practice, so that

$$h_{\rm rms} = \frac{\sqrt{\pi} N h_0}{8}. \tag{A17}$$

From this equation, we can extract h_0 as

$$h_0 = \frac{8 h_{\rm rms}}{\sqrt{\pi} N}. \tag{A18}$$

The average contrast, denoted as $\mathscr{C}$, in the DH, using equation (A14) can be written as

$$\mathscr{C} = \pi \left(\frac{8 h_{\rm rms}}{N\lambda}\right)^2. \tag{A19}$$

Assuming uniformly distributed errors (Ruane et al. 2020), we can define the minimum DM surface motion enabled, $h_{\rm min}$, such that

$$h_{\rm rms} = h_{\rm min}/\sqrt{12}. \tag{A20}$$

The average contrast in the DH, is finally

$$\mathscr{C} = \frac{16\pi}{3}\left(\frac{h_{\rm min}}{N\lambda}\right)^2. \tag{A21}$$

This paper has been typeset from a TEX/LATEX file prepared by the author.